Title

1H-13C independently tuned radiofrequency surface coil applied for in vivo hyperpolarized MRI

Journal

Magnetic Resonance in Medicine, 76(5)

ISSN

0740-3194

Authors

Cao, Peng
Zhang, Xiaoliang
Park, Ilwoo
et al.

Publication Date

2016-11-01

DOI

10.1002/mrm.26046

Peer reviewed

HHS Public Access

Author manuscript

Magn Reson Med. Author manuscript; available in PMC 2017 November 01.

Published in final edited form as:

Magn Reson Med. 2016 November ; 76(5): 1612–1620. doi:10.1002/mrm.26046.

^{1}H-^{13}C Independently Tuned RF Surface Coil Applied for In vivo Hyperpolarized MRI

Peng Cao[1], **Xiaoliang Zhang**[1], **Ilwoo Park**[1], **Chloe Najac**[1], **Sarah J. Nelson**[1], **Sabrina Ronen**[1], and **Peder E. Z. Larson**[1,*]

[1]Department of Radiology and Biomedical Imaging, University of California at San Francisco, San Francisco, CA, USA

Abstract

Purpose—To develop a lump-element double-tuned common-mode-differential-mode (CMDM) radiofrequency (RF) surface coil with independent frequency tuning capacity for MRS and MRI applications.

Methods—The presented design has two modes that can operate with different current paths, allowing independent frequency adjustment. The coil prototype was tested on the bench and then examined in phantom and in vivo experiments.

Results—Standard deviations of frequency and impedance fluctuations measured in one resonator, while changing the tuning capacitor of another resonator, were less than 13 kHz and 0.55Ω. The unloaded S21 was −36 dB and −41 dB, while the unloaded Q factor was 260 and 287, for ^{13}C and ^{1}H, respectively. In vivo hyperpolarized ^{13}C MR spectroscopy data demonstrated the feasibility of using the CMDM coil to measure the dynamics of lactate, alanine, pyruvate and bicarbonate signal in a normal rat head along with acquiring ^{1}H anatomical reference images.

Conclusion—Independent frequency tuning capacity was demonstrated in the presented lump-element double-tuned CMDM coil. This CMDM coil maintained intrinsically decoupled magnetic fields, which provided sufficient isolation between the two resonators. The results from in vivo experiments demonstrated high sensitivity of both the ^{1}H and ^{13}C resonators.

Keywords

RF coil; tuning; double-tuned; common-mode-differential-mode; CMDM; carbon-13; ^{13}C; hyperpolarization

Introduction

The recent advances of heteronuclear molecular magnetic resonance imaging (MRI) such as hyperpolarized carbon-13 (^{13}C) (1–5), hyperpolarized xenon-129 (^{129}Xe) (6–8) and other hyperpolarized and non-hyperpolarized heteronuclei (9–12) have drawn increasing interest to the technical development of efficient double-tuned RF coils. Hyperpolarized ^{13}C

*Correspondence to: Peder E. Z. Larson, Department of Radiology, University of California at San Francisco, San, Francisco, CA, USA, Address: 1700 4th Street, San Francisco CA 94158, Phone: 415-514-4876, peder.larson@ucsf.edu.

imaging provides unique real-time metabolic information and, therefore, is of particular interest in cancer applications such as tumor staging and monitoring treatment response (3,13–15). Hyperpolarized ^{129}Xe is another heteronuclear MRI method with high sensitivity and has been successfully used in clinical trials (6). In addition, sodium-23 (^{23}Na) and phosphorous-31 (^{31}P) MRI and magnetic resonance spectroscopy (MRS) in thermal equilibrium have also been used in the investigation of brain pathology (11,12,16). All these heteronuclear molecular MRI studies require heteronuclear RF coils to produce data with high sensitivity and ^{1}H RF coils to acquire ^{1}H images for reference as well as to facilitate B_0 shimming.

In the small-scale double-tuned surface coil design, the lump-element is widely used, even at the relatively high magnetic field strength of 7T. Meanwhile, double-tuned coils have to address the problem of magnetic field coupling of two resonators. Solutions for the lump-element double-tuned surface coil generally fall into two types of coil design. The first are coil designs that employ coupled magnetic fields, such as a multiple pole coil (17,18), a transformer-coupled coil (19) and a recently-developed decoupled concentric rings coil (20,21) (as illustrated in Figure 1a), where an additional RF choke is used to decouple the two resonators. The second type of coil design uses a combination of two surface coils with intrinsically decoupled magnetic fields, i.e., the directions of magnetic flux are orthogonal (22). The example in Figure 1b is a combination of a butterfly surface coil and a single-turn surface coil, which falls into the second category. The first type of design usually consists of two resonators in a single surface coil, while the second type of design is equivalent to two independently working surface coils.

It is possible to build a single surface coil with two decoupled magnetic fields. Examples are the common-mode-differential-mode (CMDM) surface coil and other multi-mode surface coils. For lump-element surface coil design at high fields, distributing the capacitor and splitting the loop allows high-frequency resonators to be implemented using practically available capacitor values (i.e., > 1 pF). Interestingly, a butterfly surface coil becomes a CMDM surface coil with these modifications, as illustrated in Figure 1c and d. The multi-mode surface or half volume coils have long been used in building quadrature ^{1}H coils (23–26), utilizing the fact that they support two intrinsically decoupled magnetic fields. The double-tuned CMDM surface coil design has also been recently demonstrated using microstrip transmission lines as resonators (27–29). Despite the advantages, one practical concern of the CMDM surface coil is the inability of two resonators to be tuned independently in conventional structure. This can make the coil design very challenging and cumbersome, especially when designing multi-channel surface coil arrays. Independent tuning capacity can greatly ease design, construction, production and operation of double-tuned RF coils.

In this study, we aimed to develop a lump-element double-tuned CMDM surface coil with independent frequency tuning capacity for ^{1}H and ^{13}C resonators. The developed CMDM surface coil maintained the intrinsically decoupled magnetic fields, which provided sufficient isolation between the two resonant modes. The coil prototype was tested on the bench, and then examined by ^{1}H and ^{13}C MR phantom experiments. Finally, the

performance of this coil was further validated by an in vivo hyperpolarized ^{13}C study with normal rat head and corresponding ^{1}H anatomical reference images.

Methods

Coil design

Figures 1d and 2a–c show the circuit diagram of the presented coil design. The presented design had two independent modes that can operate at two different frequencies with different current paths (i_1 and i_2 in Figure 1d). For the common mode (Figure 1d, left), two inner loops together formed a butterfly coil. For the differential mode (Figure 1d, right), the big outer loop was configured as a single-turn surface coil. Furthermore, the splitting capacitors C_S and the tuning capacitors C_{T1} and C_{T2} (Fig. 2a) were arranged in a way that one tuning capacitor can only affect one resonant mode. The driving circuits for the common mode and differential mode are shown in Figure 2b. A virtual 'ground' for driving the differential mode was essentially needed for eliminating an adverse electric potential between the outer conductors of two coaxial cables.

As shown in Figure 2c, a saddle coil shape with semicircular transverse profile was chosen to match the curved surface of a rat head. The dimensions of the coil prototype were 13 mm (height) ×28 mm (width) × 44 mm (length). The common mode was configured as the ^{1}H resonator (i.e., tuned to 298.06 MHz, the ^{1}H Larmor frequency at 7T), and the differential mode was configured as the ^{13}C resonator (i.e., tuned to 74.96 MHz, the ^{13}C Larmor frequency at 7T). It should be noted that such sole coil was equivalent to a butterfly coil for the ^{1}H resonator and a saddle coil for the ^{13}C resonator. In this coil prototype, all trimmers for tuning and matching were JOHANSON 80H85 non-magnetic trimming capacitors. The C_{T1} and C_{M2} had the tuning range of 1.5 to 19 pF, while the tuning range of C_{M1} and C_{T2} was 0.6 to 0.95 pF (i.e., a 1.5 −19 pF trimmer and a 1 pF capacitor in series) and 21.5 to 39 pF (i.e., a 1.5 −19 pF trimmer and a 20 pF capacitor in parallel), respectively. All fixed capacitors were from JOHANSON high Q non-magnetic ceramic capacitors designer kit (E-Series, EIA 1111). Two C_S were 20.2 pF each, and two C_D were 40 pF each.

Circuit analysis

According to Kirchhoff's voltage law for two inner coil loops and one auxiliary capacitor loop (in Figure 2a), the presented coil circuit can be described as

$$\begin{cases} -j\omega L_1 I_1+\frac{j}{\omega C_S}(I_1-I_3)+\frac{j}{\omega C_{T1}}(I_1+I_2)-j\omega L_2(I_1+I_2)=0 \\ -j\omega L_1 I_2+\frac{j}{\omega C_S}(I_2+I_3)+\frac{j}{\omega C_{T1}}(I_1+I_2)-j\omega L_2(I_1+I_2)=0 \\ \frac{j}{\omega C_{T2}}I_3+\frac{j}{\omega C_S}(I_3+I_2)+\frac{j}{\omega C_S}(I_3-I_1)=0 \end{cases} \quad \text{Eq. 1}$$

where C_S is the splitting capacitors, C_{T1} is the tuning capacitor for differential mode and L_1 and L_2 are the equivalent inductors on the outer loops and the central conductor, as defined in Figure 2a. Assuming the distribution of common mode (CM) current follows the

illustration of i_1 in Figure 1d (left), i.e., let $I_1 = I_2$ in Eq. 1, the resonant frequency is given by

$$\omega_{CM} = \sqrt{\frac{\frac{1}{C_S} + \frac{2}{C_{T1}}}{L_1 + 2L_2}} \quad \text{Eq. 2}$$

For each inner loop in common mode, Eq.2 indicates that the total capacitor is C_S and $\frac{C_{T1}}{2}$ in series, while the total inductor is L and 2L in series. There is no current flow through the tuning capacitor C_{T2}, i.e., C_{T2} cannot affect the resonant frequency of common mode. Utilizing Kirchhoff's voltage law and assuming the distribution of differential mode (DM) current follow the illustration of i_2 in Figure 1d (right), i.e., let $I_1 = -I_2$ in Eq. 1, resonant frequency is given by

$$\omega_{DM} = \frac{1}{\sqrt{\left(\frac{C_S}{2} + C_{T2}\right) \cdot 2L_1}} \quad \text{Eq. 3}$$

where C_{T2} is the tuning capacitor for differential mode. For the outer loop in differential mode, Eq.3 indicates that the total capacitor is equivalent to $\frac{C_S}{2}$ and C_{T2} in parallel, while the total inductance is $2L_1$. There is no current flow through the central conductor nor C_{T1}, i.e., C_{T1} cannot affect the resonant frequency of differential mode. Eqs.2 and 3 clearly show that resonant frequencies of common mode and differential mode can be adjusted independently via C_{T1} and C_{T2}.

Bench test

For the tuning dependency measurement, a network analyzer with full two ports (Agilent, E5071C) was used. The frequency span was set as 100 kHz and the number of points for frequency sweeping was 20000, allowing a nominal resolution of 5 Hz/point. The resonant frequency was detected automatically by searching the minimum value of the magnitude S11 (which identifies the resonant mode) within the span (i.e., 100 kHz), while the impedance at the resonant frequency was measured on the smith chart.

S11, S21 (which measures the isolation between ^{1}H and ^{13}C channels) and Q (i.e., the quality factor that measures the loss of coil) were measured under unloaded, lightly loaded and heavily loaded conditions, using a tube containing ethylene glycol (relative permittivity = 37.0 at 20 °C) and a soft water bag as loadings. The frequency span was set as 20 MHz. The center frequency was set as 298.06 MHz and 74.96 MHz for measurements on ^{1}H and ^{13}C resonators, respectively. The Q factor was calculated as $Q = 2\frac{\text{bandwidth}_{S11=-3\,dB}}{\textit{center frequency}}$.

MRI protocol

All MR experiments were performed on a 7T whole-body MRI scanner (GE Healthcare, Waukesha, WI). The ^{1}H-^{13}C phantom was made using a 21.7-mm-diameter cylinder syringe

that was filled with ethylene glycol ($HOCH_2CH_2OH$, anhydrous, 99.8%, Sigma-Aldrich, St. Louis, Missouri). For phantom experiment, a gradient-echo (GRE) ^1H imaging was first acquired with TE/TR = 2.5/100 ms, nominal flip angle = 30°, FOV = 80 × 80 mm^2, matrix size = 256 × 128 and zero filled to 256 × 256, slice thickness = 3 mm, number of excitation (NEX) = 1 and readout bandwidth = 31.25 Hz. Thirty axial, sagittal and coronal slices were acquired within 32 s. In addition, two GRE ^1H scans with nominal flip angle = 10° and 20°, respectively, were acquired to evaluate the B_1+ field of the ^1H resonator using the following parameters: TE/TR = 2.6/150 ms, FOV = 60 × 60 mm^2, matrix size = 256 × 256, slice thickness = 2 mm, 23 contiguous slices, NEX = 4 and readout bandwidth = 62.5 Hz. To probe the B_1+ field of the ^{13}C resonator, two 3D chemical shift images were acquired with nominal flip angle = 20° and 40°, respectively with the following parameters: TE/TR = 2.3/1000 ms, voxel size = 3 × 3 × 3 mm^3, matrix size = 8 × 8 × 14, slice thickness = 42 mm, NEX = 1 and readout bandwidth = 5000 Hz.

An additional phantom experiment was performed with the use of a double-tuned quadrature volume coil. The double-tuned quadrature volume coil consisted of 8 by 8 alternately placed λ/2 and λ/4 microstrip resonators as ^1H and ^{13}C elements (30). The inner diameter and length of this volume coil was 52 mm and 101 mm, respectively (30). ^1H and ^{13}C imaging parameters were made identical to those used for the experiments with the proposed double-tuned surface coil for comparison.

For the in vivo experiment, the above mentioned three-plane and multi-slice GRE ^1H imaging was preformed, lasting 32 s. Non-selective dynamic spectroscopy data (readout bandwidth = 5000 Hz and sampling points = 2048) were acquired following a bolus injection of approximately 3 mL hyperpolarized [1-^{13}C]-pyruvate solution (80 mM), produced using SpinLab (GE Healthcare, Niskayuna, New York). The detailed descriptions for preparing hyperpolarized [1-^{13}C]-pyruvate and polarization process can be found elsewhere (31,32).

Data analysis

In order to measure the B_1+ (i.e., the B1 field in transmission) maps indirectly, the double angle method (33–35) was used to estimate the flip-angle maps for both resonators. The voxel-wise flip angle was calculated as

$$B_1^{flip\ angle} = \arccos\left(\frac{S_{2\alpha}}{2S_\alpha}\right) \quad \text{Eq. 4}$$

where $S_{2\alpha}$ and S_α are the magnitude signal of the images or the area under the spectral peaks that were acquired with nominal flip angle of 2α and α, respectively. Before the ^1H flip-angle calculation, 3D ^1H $S_{2\alpha}$ and S_α datasets were filtered by a 2D median filter in x-y plane with a window size of 10 × 10 followed by a 1D median filter along z dimension with a window length of 5. While ^{13}C $S_{2\alpha}$ and S_α datasets were not filtered. The flip-angle maps were masked by thresholding S_α with threshold level = 10% and 50% of the maximum intensities for ^1H and ^{13}C datasets, respectively.

No filter was used for the ^{1}H MR images presented. The image brightness and contrast were adjusted automatically in ImageJ software (http://imagej.nih.gov/ij/). For the spectroscopic phantom imaging, no spatial or spectral filter was used. The phantom spectra were displayed in magnitudes. For in vivo spectroscopy, the post-processing included a truncation of the first 8 points of free induction decay and an apodization using a 30 Hz line broadening filter. The real part of in vivo spectra was presented.

Results

Bench test

Figure 2d shows the tuning dependency measurement. First, the ^{13}C resonator as the differential mode was tuned over a range of resonance frequencies from 74 to 86 MHz by adjusting C_{T2} from 25 to 35 pF (Figure 2d). Over this tuning range, the ^{1}H common mode resonator remained relatively stable, with standard deviations of 1.8, 1.4, 0.3, 0.7 and 0.8 kHz in resonance frequency and 0.08, 0.06, 0.16, 0.10 and 0.3Ω in impedance, as tested at 332, 316, 298 and 295 MHz, respectively. Similarly, the ^{1}H resonator as the common mode was tuned over a range of resonance frequencies from 280 to 380 MHz by adjusting C_{T1} from 2 to 19 pF (Figure 2e). Over this tuning range, the ^{13}C differential mode resonator remained relatively stable, with standard deviations of 6.4, 1.7, 13.0 and 6.0 kHz in resonance frequency and 0.53, 0.11, 0.55 and 0.43Ω in impedance, as tested at 79, 78, 77, 76 and 74 MHz. In summary, adjusting the tuning capacitor of one resonator, standard deviations of frequency and impedance fluctuations measured in the other resonator were less than 13 kHz and 0.55Ω. Therefore, tuning on each resonator was independent of another resonator with our circuit design.

Supporting Figure S1 shows the typical S11 and Q results for both ^{1}H and ^{13}C resonators. The unloaded S11 was −35 dB and −40 dB, the unloaded S21 −32 dB and −30 dB, and the unloaded Q factor 260 and 278 for ^{13}C and ^{1}H, respectively. The lightly loaded S11 was −43 dB and −43 dB, the lightly loaded S21 −32 dB and −27 dB, and the lightly loaded Q factor 260 and 218 for ^{13}C and ^{1}H, respectively. The heavily loaded S11 was −37 dB and −31 dB, the heavily loaded S21 −21 dB and −17 dB, and the heavily loaded Q factor 198 and 118 for ^{13}C and ^{1}H, respectively. The relatively low S21 and high Q factors supported the intrinsic decoupling of two magnetic fields. Furthermore, as shown in Supporting Figure S2, probing with a sniffer coil identified the two resonant modes, and the intrinsic decoupling of two magnetic fields was confirmed by showing the orthogonal magnetic flux.

Phantom

Figure 3a shows gradient-echo ^{1}H images and ^{13}C spectra from a cylindrical ethylene glycol phantom. The intensity variations in ^{1}H images and ^{13}C spectra represented the typical behavior of the surface coil that was working at both transition and reception. It should be noted that the ^{13}C resonator (in Figure 3b) produced a relatively homogeneous flip-angle map, which reflected the B_1+ field, within the region of interest, due to the saddle shape of the coil (in Figure 2c). Figure 3c shows an additional phantom experiment that was performed with the use of a double-tuned quadrature volume coil. The presented double-tuned surface coil provided much higher local sensitivity (i.e., Figure 3a vs. Figure 3c) than

the double-tuned quadrature volume coil but exhibited inhomogeneous B_1 fields as expected (in Figure 3b). The three-plane and multi-slice ^{1}H images of the phantom can be found in Figure 4.

Preliminary in vivo data from a rat head

Figure 5 shows gradient-echo ^{1}H images and hyperpolarized ^{13}C spectra from a normal rat head. The gradient-echo images allowed the visualization of various regions of the rat brain, including the cortex and the thalamus in midbrain. The in vivo hyperpolarized ^{13}C MR spectroscopy demonstrated the capability of measuring the dynamics of lactate, alanine, pyruvate and bicarbonate signal. Alanine signal most likely came from muscles around the head (36). The high sensitivity of these signals suggested that the ^{13}C resonator had good sensitivity. The axial and sagittal multi-slice ^{1}H images can be found in Figure 6.

Discussion

Independent frequency tuning

In the current study, we have demonstrated the independent frequency tuning capacity of the newly developed lump-element double-tuned CMDM coil. Using a circuit analysis, we demonstrated that one tuning capacitor could be used to adjust the resonant frequency of one mode without having current flowing in another tuning capacitor for the other mode. The bench test result clearly showed that the two resonant frequencies could be tuned independent of each other, verifying the circuit analysis. In principle, such independent frequency tuning or adjustment should be broadband; hence the presented double-tuned coil design can be potentially applied to other heteronuclei, such as ^{23}Na (gyromagnetic ratio $\gamma = 70.8 \times 10^6$ rad·s^{-1}·T^{-1}), ^{31}P ($\gamma = 108.4 \times 10^6$ rad·s^{-1}·T^{-1}), nitrogen-15 (^{15}N, $\gamma = -27.1 \times 10^6$ rad·s^{-1}·T^{-1}) and ^{129}Xe ($\gamma = -74.5 \times 10^6$ rad·s^{-1}·T^{-1}) and other heteronuclear MR applications that require high local sensitivity. For example, in addition to the hyperpolarized ^{13}C ($\gamma = -67.3 \times 10^6$ rad·s^{-1}·T^{-1}) and ^{129}Xe applications, it may be feasible to use the present coil for hyperpolarized ^{15}N MRI applications because ^{15}N generally has a long lasting hyperpolarized state. pH imaging with hyperpolarized ^{15}N has been recently demonstrated with the use of dynamic nuclear polarization (DNP) (9) and signal amplification by reversible exchange (SABRE) polarization techniques (10). For the field strength of 7T, as demonstrated by the presented study, the lump-element design of the ^{1}H resonator should still be valid for small-scale coils (i.e., < 5 cm) and small animal applications. For higher field MRI (i.e., > 7T), the presented lump-element design of ^{1}H resonators should be modified, e.g., using the microstrip transmission lines as resonators (27–29), due to the difficulty of implementing lump-element resonators at high frequencies. In summary, the presented double-tuned RF surface coil design can be extended to a broad range of heteronuclear MRI applications; though each implementation shall be subject to the coil size and the resonant frequencies with regard to field strength and gyromagnetic ratios.

Compared with double-tuned quadrature volume coils, the presented double-tuned surface coil provided relatively high local sensitivity for heteronuclear MRI, but involved inhomogeneous B_1 fields. The ideal configuration of RF coils would be a double-tuned quadrature volume coil for transmission with homogeneous B_1 fields and a double-tuned

surface coil with optimal local sensitivities for reception. It should be noted that the differential mode in the presented design, i.e., the ^{1}H resonator which performed as a butterfly coil, may possess a smaller orthogonal field component but a higher noise level due to an exposed area at the open side of the coil. A slightly larger coil may be needed if the ^{1}H image of the deep brain is desired, and/or an additional ^{1}H resonator (and decoupling circuit) could be used to compensate the sensitivity loss in the exposed area.

Intrinsically decoupled two magnetic fields

The relatively low S21 and high Q factor of the presented coil showed the sufficient isolation between two resonators, most likely due to the intrinsic decoupling of two magnetic fields. This observation was also consistent with the S21 measurements of other CMDM coils, including the double-tuned microstrip CMDM coil (29) and the quadrature ^{1}H CMDM coil (23). The bench test of the present coil prototype showed that two inner loops were well balanced, and as a result, no fine adjustment was performed. In practice, two splitting capacitors (i.e., two C_S) can be adjusted individually in order to keep the resonant frequencies of the two inner loops same.

In the presented coil, balance-driving capacitors (i.e., two C_D) were used for the common mode. It should be noted that most RF chokes or baluns (balun: balance–to-unbalance) in RF coil design are narrowband. In the presented double-tuned coil, a balun had to work for two frequencies of both modes. The balance-driving capacitors (i.e., two C_D) allowed a virtual ‘ground’ for driving the differential mode in a simple structure. Alternatively, the common mode can be driven by an inductive coupling loop (23,29), which may involve more components. To eliminate the residual electric potential from unbalances between two C_D or two C_S, an RF choke was empirically added to the coaxial cable of the port for driving the common mode, and two coaxial cables of two ports were twitched together. These treatments helped maintain a low unloaded S21 (i.e., < -30 dB) on the bench.

Possible extensions

The independent frequency tuning and electronic driving circuit presented in this study using the lump-element double-tuned CMDM coil could be applied to other CMDM coils. There is an implicit similarity between the presented lump-element CMDM coil and the previously proposed microstrip CMDM coils (23,29). In microstrip CMDM coil, the shared outer conductor of two microstrip resonators was comparable to the central conductor of the presented lump-element CMDM coil. The equivalent circuit for mircrostrip CMDM coil would be similar to that for the presented coil. The independent frequency tuning and electronic driving circuit, i.e., the arrangement of capacitors C_{T1}, C_{T2}, C_S and C_D, may be used in the microstrip CMDM coil.

With advantages of independent frequency tuning and intrinsically decoupled magnetic fields, the presented double-tuned CMDM coil could serve as a building block for double-tuned phase array coils. When building a phase array coil, channel decoupling is essential. It has been demonstrated that the magnetic wall decoupling technique can effectively decouple the tightly coupled elements of the phase array coil (37). Additionally, the magnetic wall decoupling has a broadband frequency decoupling capability, which is particularly useful for

the double-tuned coil array design where two separated frequencies are involved. In practice, intersecting double-tuned CMDM resonators with magnetic walls may be particularly effective for achieving sufficient decoupling in building a double-tuned phased array coil using double-tuned CMDM coils.

Conclusion

We developed a lump-element double-tuned CMDM coil with independent frequency tuning capacity for ^{1}H and ^{13}C resonators. This CMDM coil maintained the intrinsically decoupled magnetic fields, which provided sufficient isolation between the two resonators. The independent tuning capacity greatly eased the design, construction, production and operation of our double-tuned coil. The in vivo hyperpolarized ^{13}C MR spectroscopy data acquired with the CMDM coil demonstrated the feasibility of assessing the dynamics of lactate, alanine, pyruvate and bicarbonate signal in a normal rat head with high sensitivity. With the use of appropriate decoupling mechanism, extensions of this double-tuned CMDM coil to double-tuned multichannel RF coil arrays is also possible.

Supplementary Material

Refer to Web version on PubMed Central for supplementary material.

Acknowledgments

The authors want to thank Lucas Carvajal for helping on the MRI experiment. This work is supported by NIH grants R00EB012064, R01EB016741, P01CA118816, P41EB013598, R01CA154915, R01CA172845 and R01EB008699.

References

1. Ardenkjaer-Larsen JH, Fridlund B, Gram A, Hansson G, Hansson L, Lerche MH, Servin R, Thaning M, Golman K. Increase in signal-to-noise ratio of > 10,000 times in liquid-state NMR. Proceedings of the National Academy of Sciences of the United States of America. 2003; 100(18):10158–10163. [PubMed: 12930897]
2. Keshari KR, Wilson DM. Chemistry and biochemistry of 13C hyperpolarized magnetic resonance using dynamic nuclear polarization. Chemical Society reviews. 2014; 43(5):1627–1659. [PubMed: 24363044]
3. Kurhanewicz J, Vigneron DB, Brindle K, Chekmenev EY, Comment A, Cunningham CH, Deberardinis RJ, Green GG, Leach MO, Rajan SS, Rizi RR, Ross BD, Warren WS, Malloy CR. Analysis of cancer metabolism by imaging hyperpolarized nuclei: prospects for translation to clinical research. Neoplasia. 2011; 13(2):81–97. [PubMed: 21403835]
4. Nikolaou P, Goodson BM, Chekmenev EY. NMR hyperpolarization techniques for biomedicine. Chemistry. 2015; 21(8):3156–3166. [PubMed: 25470566]
5. Hirsch ML, Kalechofsky N, Belzer A, Rosay M, Kempf JG. Brute-Force Hyperpolarization for NMR and MRI. Journal of the American Chemical Society. 2015; 137(26):8428–8434. [PubMed: 26098752]
6. Mugler JP 3rd, Altes TA. Hyperpolarized 129Xe MRI of the human lung. Journal of magnetic resonance imaging : JMRI. 2013; 37(2):313–331. [PubMed: 23355432]
7. Roos JE, McAdams HP, Kaushik SS, Driehuys B. Hyperpolarized Gas MR Imaging: Technique and Applications. Magnetic resonance imaging clinics of North America. 2015; 23(2):217–229. [PubMed: 25952516]

8. Liu Z, Araki T, Okajima Y, Albert M, Hatabu H. Pulmonary hyperpolarized noble gas MRI: recent advances and perspectives in clinical application. European journal of radiology. 2014; 83(7):1282–1291. [PubMed: 24840481]
9. Jiang W, Lumata L, Chen W, Zhang S, Kovacs Z, Sherry AD, Khemtong C. Hyperpolarized 15N-pyridine derivatives as pH-sensitive MRI agents. Scientific reports. 2015; 5:9104. [PubMed: 25774436]
10. Shchepin RV, Truong ML, Theis T, Coffey AM, Shi F, Waddell KW, Warren WS, Goodson BM, Chekmenev EY. Hyperpolarization of "Neat" Liquids by NMR Signal Amplification by Reversible Exchange. The journal of physical chemistry letters. 2015; 6(10):1961–1967. [PubMed: 26029349]
11. Paling D, Golay X, Wheeler-Kingshott C, Kapoor R, Miller D. Energy failure in multiple sclerosis and its investigation using MR techniques. Journal of neurology. 2011; 258(12):2113–2127. [PubMed: 21660561]
12. Thulborn KR, Gindin TS, Davis D, Erb P. Comprehensive MR imaging protocol for stroke management: tissue sodium concentration as a measure of tissue viability in nonhuman primate studies and in clinical studies. Radiology. 1999; 213(1):156–166. [PubMed: 10540656]
13. Park I, Larson PE, Zierhut ML, Hu S, Bok R, Ozawa T, Kurhanewicz J, Vigneron DB, Vandenberg SR, James CD, Nelson SJ. Hyperpolarized 13C magnetic resonance metabolic imaging: application to brain tumors. Neuro-oncology. 2010; 12(2):133–144. [PubMed: 20150380]
14. Albers MJ, Bok R, Chen AP, Cunningham CH, Zierhut ML, Zhang VY, Kohler SJ, Tropp J, Hurd RE, Yen YF, Nelson SJ, Vigneron DB, Kurhanewicz J. Hyperpolarized 13C lactate, pyruvate, and alanine: noninvasive biomarkers for prostate cancer detection and grading. Cancer research. 2008; 68(20):8607–8615. [PubMed: 18922937]
15. Nelson SJ, Kurhanewicz J, Vigneron DB, Larson PE, Harzstark AL, Ferrone M, van Criekinge M, Chang JW, Bok R, Park I, Reed G, Carvajal L, Small EJ, Munster P, Weinberg VK, Ardenkjaer-Larsen JH, Chen AP, Hurd RE, Odegardstuen LI, Robb FJ, Tropp J, Murray JA. Metabolic imaging of patients with prostate cancer using hyperpolarized [1-(1)(3)C]pyruvate. Science translational medicine. 2013; 5(198):198ra108.
16. Schepkin VD, Bejarano FC, Morgan T, Gower-Winter S, Ozambela M Jr, Levenson CW. In vivo magnetic resonance imaging of sodium and diffusion in rat glioma at 21. 1 T. Magn Reson Med. 2012; 67(4):1159–1166. [PubMed: 21748798]
17. Schnall MD, Subramanian VH, Leigh JS. The Application of over-Coupled Tank-Circuits to Nmr Probe Design. J Magn Reson. 1986; 67(1):129–134.
18. Eleff SM, Schnall MD, Ligetti L, Osbakken M, Subramanian VH, Chance B, Leigh JS. Concurrent Measurements of Cerebral Blood-Flow, Sodium, Lactate, and High-Energy Phosphate-Metabolism Using F-19, Na-23, H-1, and P-31 Nuclear Magnetic-Resonance Spectroscopy. Magn Reson Med. 1988; 7(4):412–424. [PubMed: 3173056]
19. Fitzsimmons JR, Brooker HR, Beck B. A transformer-coupled double-resonant probe for NMR imaging and spectroscopy. Magn Reson Med. 1987; 5(5):471–477. [PubMed: 3431409]
20. Alecci M, Romanzetti S, Kaffanke J, Celik A, Wegener HP, Shah NJ. Practical design of a 4 Tesla double-tuned RF surface coil for interleaved H-1 and Na-23 MRI of rat brain. J Magn Reson. 2006; 181(2):203–211. [PubMed: 16716616]
21. Dabirzadeh A, McDougall MP. Trap Design for Insertable Second-Nuclei Radiofrequency Coils for Magnetic Resonance Imaging and Spectroscopy. Concept Magn Reson B. 2009; 35B(3):121–132.
22. Adriany G, Gruetter R. A half-volume coil for efficient proton decoupling in humans at 4 tesla. J Magn Reson. 1997; 125(1):178–184. [PubMed: 9245377]
23. Li Y, Yu BY, Pang Y, Vigneron DB, Zhang XL. Planar Quadrature RF Transceiver Design Using Common-Mode Differential-Mode (CMDM) Transmission Line Method for 7T MR Imaging. Plos One. 2013; 8(11)
24. Braum, WO.; Kristoff, JW.; Molyneaux, DA. European Patent. 1998. Multi-mode RF coil.
25. Liu, H.; Truwit, CL. United States Patent. 1999. Single circuit ladder resonator quadrature surface RF coil.

26. Peshkovsky AS, Kennan RP, Fabry ME, Avdievich NI. Open half-volume quadrature transverse electromagnetic coil for high-field magnetic resonance imaging. Magn Reson Med. 2005; 53(4): 937–943. [PubMed: 15799051]
27. Zhang X, Ugurbil K, Chen W. Microstrip RF surface coil design for extremely high-field MRI and spectroscopy. Magn Reson Med. 2001; 46(3):443–450. [PubMed: 11550234]
28. Zhang X, Ugurbil K, Chen W. A microstrip transmission line volume coil for human head MR imaging at 4T. J Magn Reson. 2003; 161(2):242–251. [PubMed: 12713976]
29. Pang Y, Zhang XL, Xie ZT, Wang CS, Vigneron DB. Common-Mode Differential-Mode (CMDM) Method for Double-Nuclear MR Signal Excitation and Reception at Ultrahigh Fields. Ieee T Med Imaging. 2011; 30(11):1965–1973.
30. Pang Y, Xie Z, Xu D, Kelley DA, Nelson SJ, Vigneron DB, Zhang X. A dual-tuned quadrature volume coil with mixed lambda/2 and lambda/4 microstrip resonators for multinuclear MRSI at 7 T. Magn Reson Imaging. 2012; 30(2):290–298. [PubMed: 22055851]
31. Hu S, Larson PEZ, VanCriekinge M, Leach AM, Park I, Leon C, Zhou J, Shin PJ, Reed G, Keselman P, von Morze C, Yoshihara H, Bok RA, Nelson SJ, Kurhanewicz J, Vigneron DB. Rapid sequential injections of hyperpolarized [1-C-13]pyruvate in vivo using a sub-kelvin, multi-sample DNP polarizer. Magn Reson Imaging. 2013; 31(4):490–496. [PubMed: 23107275]
32. Park I, Larson PE, Tropp JL, Carvajal L, Reed G, Bok R, Robb F, Bringas J, Kells A, Pivirotto P, Bankiewicz K, Vigneron DB, Nelson SJ. Dynamic hyperpolarized carbon-13 MR metabolic imaging of nonhuman primate brain. Magn Reson Med. 2014; 71(1):19–25. [PubMed: 24346964]
33. Stollberger, RWP.; McKinnon, G.; Justich, E.; Ebner, F. RF-field mapping in vivo. Proceedings of the 7th Annual Meeting of SMRM; San Francisco, USA. 1988. p. 106
34. Insko, EKBL. B1mapping. Proceedings of the 11th Annual Meeting of SMRM; Berlin, Germany. 1992. p. 4302
35. Cunningham CH, Pauly JM, Nayak KS. Saturated double-angle method for rapid B1+ mapping. Magn Reson Med. 2006; 55(6):1326–1333. [PubMed: 16683260]
36. Chang TW, Goldberg AL. The origin of alanine produced in skeletal muscle. The Journal of biological chemistry. 1978; 253(10):3677–3684. [PubMed: 649595]
37. Li Y, Xie ZT, Pang Y, Vigneron D, Zhang XL. ICE decoupling technique for RF coil array designs. Med Phys. 2011; 38(7):4086–4093. [PubMed: 21859008]

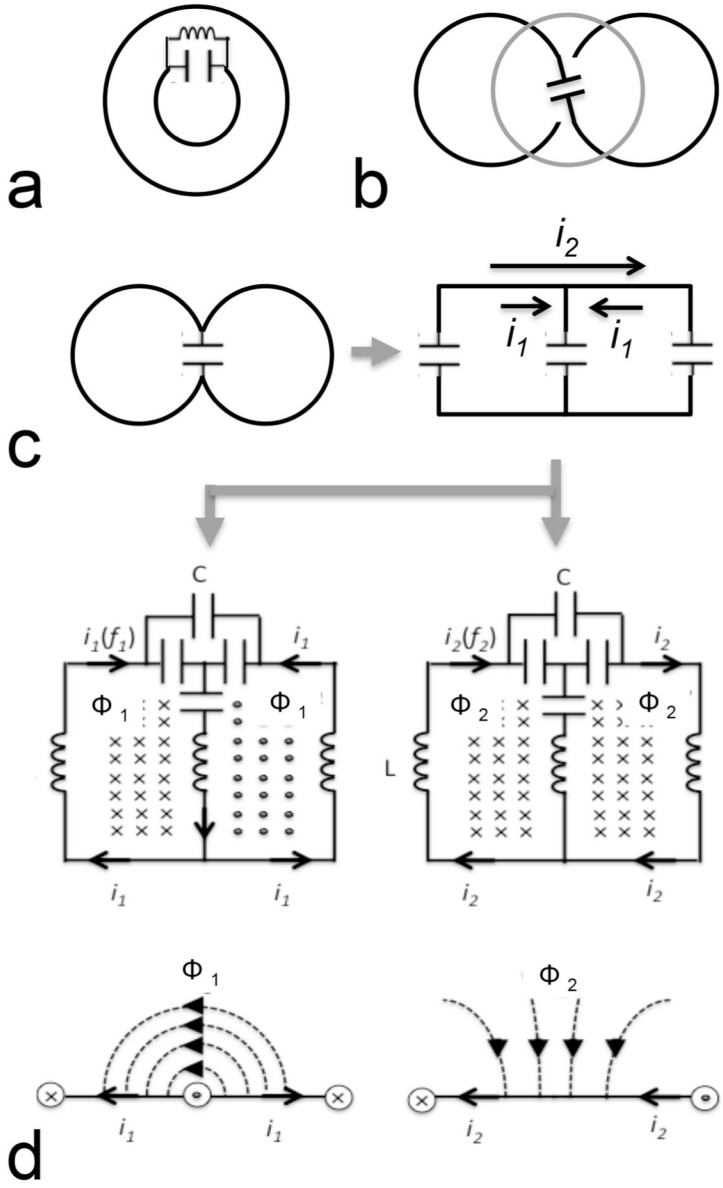

Figure 1.

(**a**) Conventional concentric rings double-tuned surface coil with a RF choke for the inner resonator. (**b**) Conventional intrinsically decoupled double-tuned surface coil, containing a butterfly coil (black) and a single-turn surface coil (gray). (**c**) Evolution from butterfly coil to the common-mode-differential-mode (CMDM) coil. By splitting the single loop of butterfly coil (left) and adding additional capacitors (right), butterfly coil becomes the CMDM coil. (**d top**) In this CMDM coil (left is common mode, right is differential mode), the currents of the two modes can operate at two different frequencies (f_1 and f_2) with different current paths, which provide a possibility of independent frequency control. The two currents (i_1 and i_2) generate two independent and intrinsically decoupled magnetic fields. (**d bottom**) Cross-sectional views of the two modes show two intrinsically decoupled magnetic fields.

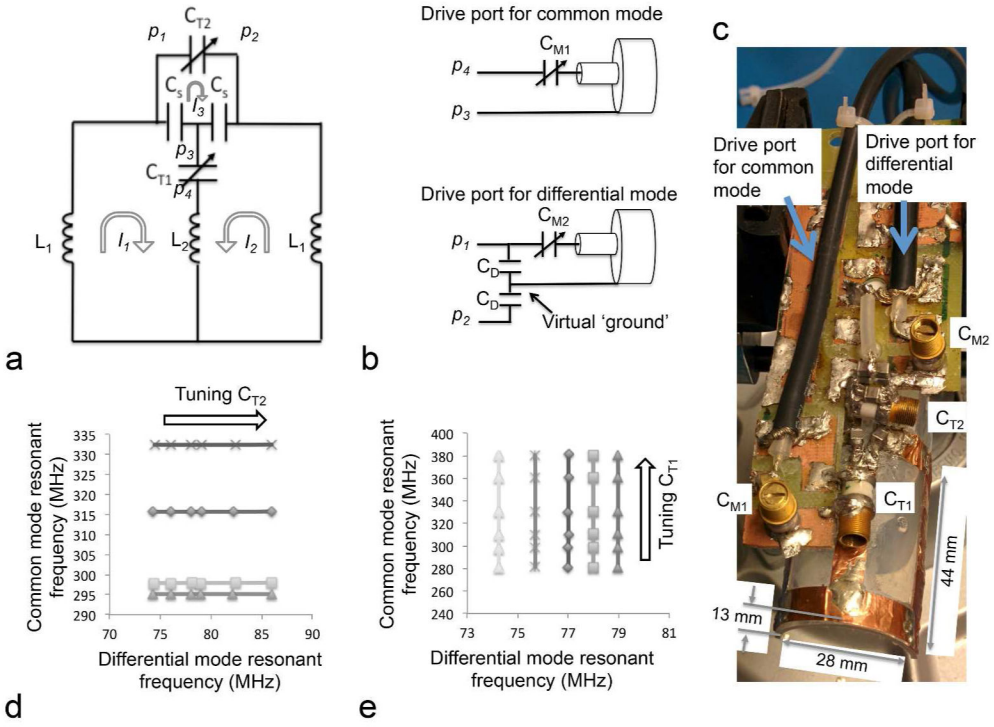

Figure 2.

(**a**) The arrangement of capacitors (C_{T1}, C_{T2}, and C_S). This arrangement allows independent frequency adjustments (via variable capacitors C_{T1} and C_{T2}) for the two resonant modes (in Fig. 1 c and d). I_1, I_2 and I_3 are currents that are used in the circuit analysis based on Kirchhoff's voltage law. (**b**) The driving circuits for the common mode and differential mode resonators. Two matching capacitors C_{M1} and C_{M2} allow impedances of two resonators to be matched to 50Ω. The balance-driving capacitors (i.e., two C_D) allow a virtual 'ground' for driving the differential mode in a simple structure. The virtual 'ground' is essentially needed for eliminating an adverse electric potential between the outer conductors of two coaxial cables. (**c**) The coil prototype for rat brain imaging at 7T. (**d** and **e**) Tuning-dependency measurement for the present double-tuned surface coil without loading. The graphes show frequencies of two modes measured by adjusting differential mode tuning capacitor (C_{T2}, in Fig. 2) only (**d**) and common mode tuning capacitor (C_{T1}, in Fig. 2) only (**e**). These results illustrate the independent frequency tuning for common mode and differential mode.

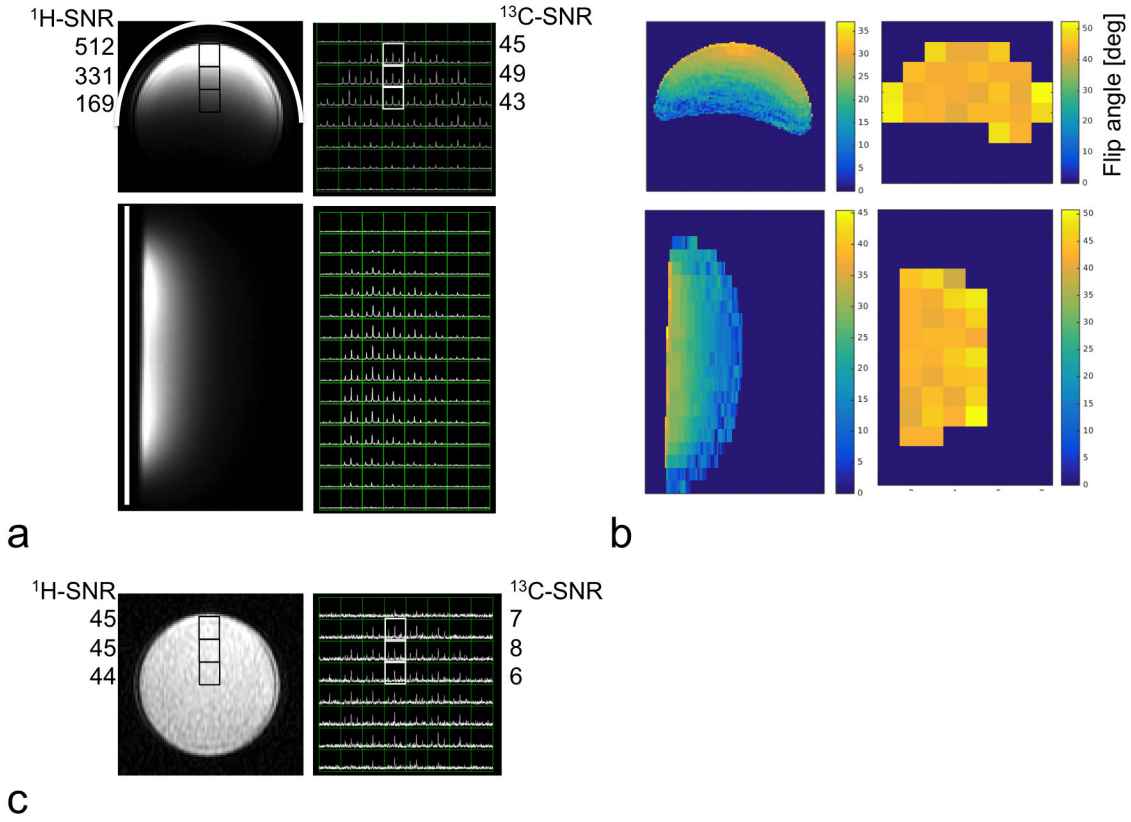

Figure 3.

MRI phantom experimental results for the presented double-tuned surface coil. (**a**) Axial and sagittal low-flip-angle gradient-echo ^{1}H images (nominal flip angle = 30°, NEX = 1) and ^{13}C spectra (nominal flip angle = 40°, NEX = 1) from a cylindrical phantom filled with ^{13}C ethylene glycol. White bold lines indicate the position of RF coil. Note that ethylene glycol has two peaks in proton spectrum, causing slight chemical shift displacements in MRI images. (**b**) B1+ maps for ^{1}H (left) and ^{13}C (right), derived from a double-flip-angle method (15° and 30° for ^{1}H images and 20° and 40° for ^{13}C spectra). (**c**) For comparison, another phantom experiment was performed with a 52-mm-diameter double-tuned quadrature volume coil, and the imaging parameters were identical to those used in (a). The presented double-tuned surface coil provided high local sensitivity but involved inhomogeneous B_1 fields.

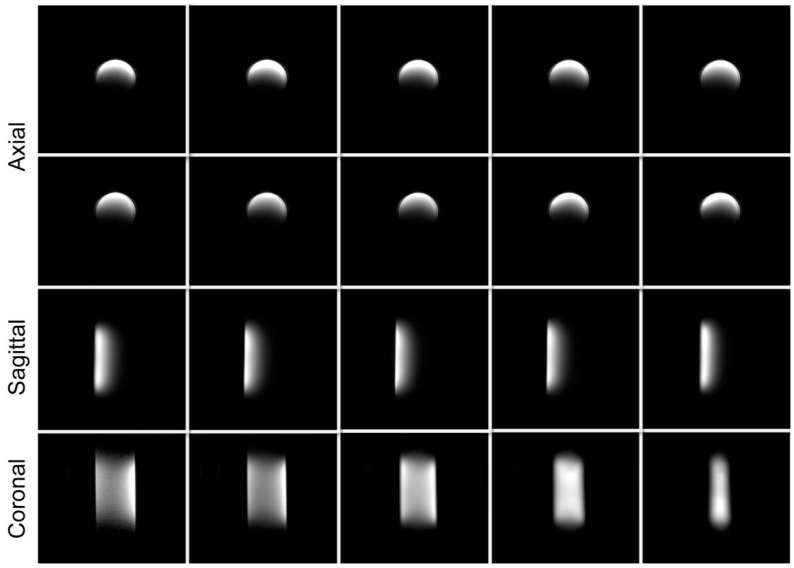

Figure 4.
Three-plane images of cylindrical ethylene glycol phantom shown in Figure 3.

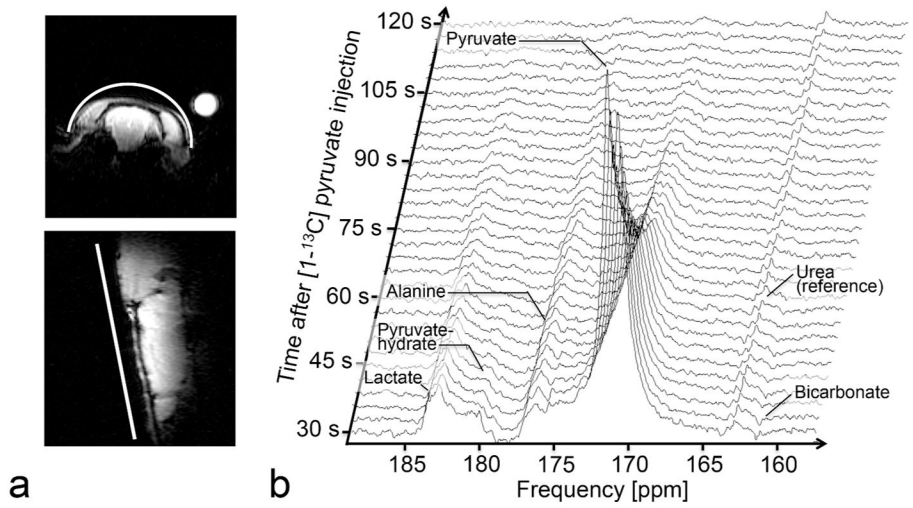

Figure 5.

(**a**) Low-flip-angle gradient-echo MRI images (nominal flip angle = 30°, NEX = 1) from a normal rat brain in an axial (top) and a sagittal (bottom) plane. White bold lines indicate the position of RF coil. The round, bright signal at the top right hand corner in the axial image is from an urea ^{13}C reference. (**b**) Hyperpolarized ^{13}C spectra (non-selective excitation, nominal flip angle = 5°, and temporal resolution = 3 s/spectrum) demonstrated the capability of measuring the dynamics of lactate, alanine, pyruvate and bicarbonate signal with high sensitivity.

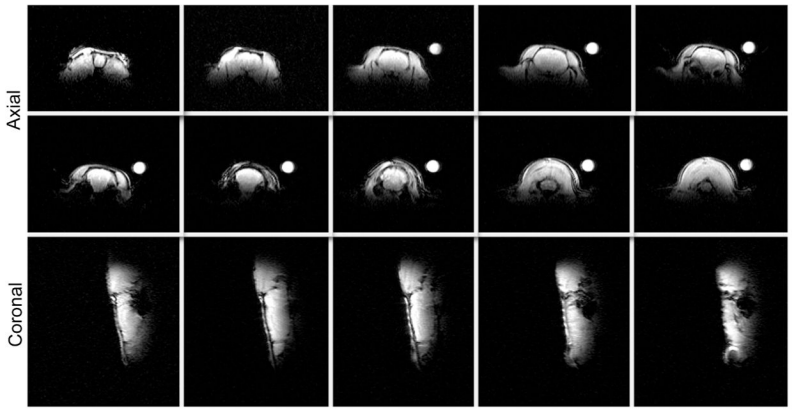

Figure 6.
Axial and sagittal multi-slice low-flip-angle gradient-echo images of normal rat brain in Figure 5.